

Interaction of plastic hinges in prestressed concrete bridges with corrugated steel webs



X.C. Chen^{a,b}, Y. Zeng^a, F.T.K. Au^{a,*}, R.J. Jiang^{c,a}

^a Department of Civil Engineering, The University of Hong Kong, Pokfulam Road, Hong Kong, China

^b Research and Technology Center, WISE-TECH Engineering Consulting Co. Ltd, Shen Zhen, China

^c Department of Civil Engineering, Shandong University, Shandong, China

ARTICLE INFO

Article history:

Received 17 December 2015

Revised 11 July 2017

Accepted 13 July 2017

Available online 27 July 2017

Keywords:

Corrugated steel web

Critical region

External tendon

Full-range structural behaviour

Plastic hinge length

Prestressed concrete

ABSTRACT

Prestressed concrete bridges with corrugated steel webs have emerged as one of the promising bridge forms. However, the presence of prestressing tendons and shear-deformable corrugated steel webs with negligible axial stiffness complicates the formation of plastic hinges under applied loading to failure. The full-range structural behaviour of these bridges and plastic hinge formation are therefore studied experimentally and numerically. The more localised flange plastic hinge caused by both web shear deformation and local flange bending interacts with the full-depth plastic hinge of such a bridge. Tests show that the full-range structural behaviour of the bridge is mainly governed by the localised flange plastic hinges. A formula is proposed to predict the equivalent interactive plastic hinge length, which helps to predict the full-range structural behaviour taking into account the presence of external prestressing tendons. Some design recommendations are also provided.

© 2017 Elsevier Ltd. All rights reserved.

1. Introduction

Concrete bridges with corrugated steel webs and external prestressing have emerged as one of the promising bridge forms for short to medium spans. Since the appearance of Cognac Bridge in France in 1986, this form of bridges has evolved and spread to other countries. Its lightness makes it ideal not only for girder bridges but also serving as the deck in cable-stayed bridges. The corrugated steel webs provide high shear resistance and obviate the need for extensive stiffeners. Because of the negligible axial stiffness of corrugated webs, the prestress can be introduced efficiently to the concrete flanges that need pre-compression. Prestressing is often achieved by both internal and external tendons. This structural form therefore provides excellent structural efficiency. Hereafter in this paper, this form of bridge is assumed unless otherwise stated.

Although various models [1,2] have been proposed to predict the static elastic behaviour of the bridge, few researchers have studied the formation of plastic hinges in these bridges and their effect on the full-range structural behaviour that covers both the pre-peak-strength and post-peak-strength responses. Plastic hinge formation is often used to describe the behaviour of concrete

beams at failure, e.g. Ho and Pam [3], Au et al. [4], Du et al. [5], Chou et al. [6], Yang et al. [7], Di Ludovico et al. [8], and Lee et al. [9], but it remains a controversial issue [10]. There are three approaches in describing the extent of plastic region: (a) the actual size of plasticity zone observed, (b) the equivalent size estimated based on a representative plastic curvature, and (c) the size of region requiring effective confinement. In Approach (a), the physical length of the actual plastic hinge region, i.e. the physical plastic hinge length l_{pc} , is defined as the length over which actual plasticity spreads. To describe the deformation capacity in Approach (b), an equivalent plastic hinge length l_p is often defined where the plastic curvature is assumed to be constant at the peak value [11]. Approach (c) by providing effective confinement will be explained later.

Studies of plastic hinges in reinforced concrete (RC) and prestressed concrete (PC) members are mostly based on experiments. Table 1 summarises various empirical formulae proposed for the equivalent plastic hinge length l_p on one side of the critical section for conventional concrete members as elaborated below. The major factors affecting the equivalent plastic hinge length include the effective or total depth of section, concrete strength, compressive axial load level, properties and areas of longitudinal and transverse steel, and distance between the critical section and point of contraflexure. As the expressions in Table 1 are taken from various sources [12–27], the symbols are adjusted for consistent presentation. The geometric properties include the distance from the

* Corresponding author.

E-mail address: francis.au@hku.hk (F.T.K. Au).

Table 1
Equivalent plastic hinge length l_p on one side of critical section.

Source	Equivalent plastic hinge length on one side	Applicable members
Baker [12]	$k_1 k_2 k_3 (z/d)^{0.25} d$	Members with unconfined concrete
Baker and Amarakone [13]	$0.8 k_1 k_3 (z/d) c$	Members confined by transverse steel
Sawyer [14]	$0.25d + 0.075z$	RC members
Corley [15]	$0.5d + 0.2\sqrt{d}(z/d)$	Beams
Mattock [16]	$0.5d + 0.05z$	Beams
Park et al. [17]	$0.5h$	Columns
Priestley and Park [18]	$0.08z + 6d_b$	Confined columns
Paulay and Priestley [19]	$0.08z + 0.022d_b f_y$	Beams and columns
Sheikh and Khoury [20]	$1.0h$	Columns under high axial loads
Bayrak and Sheikh [21]	$0.9h$ to $1.0h$	Columns
Coleman and Spacone [22]	$G_{cf} / [0.6f'_c (\epsilon_{20} + 0.8f'_c / E_c - \epsilon_c)]$	RC members
Panagiotakos and Fardis [23]	$0.18z + 0.021d_b f_y$	Beams and columns
Mendis [24]	$0.4h$	Columns
Bae and Bayrak [25]	$l_p/h = [0.3P/P_0 + 3A_s/A_g - 0.1]z/h + 0.25 \geq 0.25$	Columns
Berry et al. [26]	$0.05z + 0.1f_y d_b / \sqrt{f'_c}$	Columns
Subramanian [27]	$l_p/h = 0.9[1 + 0.5P/P_0]k_3(z/h)^{0.25}$ for $P/P_0 > 0.2$ $l_p/h = 0.25$ for $P/P_0 \leq 0.2$	Columns

critical section to the point of contra-flexure z ; the effective section depth d ; the neutral axis depth c at the ultimate moment; the section depth h of the column, and the gross area of member section A_g . The longitudinal reinforcement of sectional area A_s comprises bars of diameter d_b and yielding stress f_y . The concrete has compressive cylinder strength f'_c , peak compressive strain ϵ_c , strain ϵ_{20} corresponding to 20% of the compressive strength, and fracture energy in compression G_{cf} . The compressive axial force in the member is P , while the axial compressive strength of member without bending moment is given by $P_0 = 0.85f'_c(A_g - A_s) + f_y A_s$. The parameters used in Table 1 are: $k_1 = 0.7$ for mild steel, or 0.9 for cold-worked steel; $k_2 = 1 + 0.5P/P_0$; $k_3 = 0.6$ for $f'_c = 35.2$ MPa, or 0.9 for $f'_c = 11.7$ MPa.

Some researchers, e.g. Youssf et al. [28], have also studied the plastic hinge of concrete columns confined by fibre-reinforced polymer (FRP). Despite various formulae suggested for the equivalent plastic hinge length, no common consensus has been reached. Another related quantity by Approach (c) is the critical region length l_c in design, defined as the extent requiring effective confinement by transverse reinforcement so as to achieve the intended performance level of flexural ductility [29]. The equivalent plastic hinge length should be a fictitious extent within the critical region of a member. Clause 10.4.5 of NZS 3101 [30] recommends the critical region length or ductile detailing length to depend only on the applied compressive axial load level $P/(\lambda_r A_g f'_c)$, where the strength reduction factor λ_r is taken as 0.65 and 0.85 for unconfined and confined concrete respectively. For an RC member with $P/(\lambda_r A_g f'_c) \leq 0.25$, $0.25 < P/(\lambda_r A_g f'_c) \leq 0.5$ or $0.5 < P/(\lambda_r A_g f'_c) \leq 0.7$, its critical region length is $1.0h$, $2.0h$ or $3.0h$ respectively; or is over a region where the moment exceeds 0.8, 0.7 or 0.6 respectively of the maximum moment, whichever is larger. Paultre et al. [31] showed the critical region length to range from $1.0h$ to $2.0h$, depending on the volumetric ratio of the transverse steel and the compressive axial load level. Pam and Ho [29] observed the critical region length to increase with the compressive axial load level and concrete strength. Hence, the critical region length increases with compressive axial load level, concrete strength, longitudinal steel ratio and strength, but reduces with the transverse steel ratio.

The presence of shear-deformable corrugated steel webs with negligible axial stiffness and prestressing tendons in this kind of bridges certainly complicates the formation of plastic hinges further. While the above formulae are useful for estimation of equivalent plastic hinge length within their respective scopes, their application to the present case should be treated with care. Hence in this study, the critical region length, performance of the plastic

hinges and full-range structural behaviour of the bridges are studied.

2. Experimental programme

Some concrete beam specimens with corrugated steel webs of depth 360 mm were fabricated for testing as shown in Fig. 1. Specimens B-1 and B-2 were post-tensioned by two external 7-wire steel strands each of nominal diameter 12.7 mm and sectional area 98.7 mm². Specimen B-3 was not prestressed. Specimen B-4 was post-tensioned by two external aramid fibre reinforced polymer (AFRP) ropes each of area 54.5 mm². In Specimen B-1, the anchorages of straight strands were located at the end diaphragms at a level 110 mm above the soffit. In Specimens B-2 and B-4, the anchorages were located at the centroidal level of end diaphragms while the strands at intermediate deviator were 100 mm above the soffit. The effective prestressing forces of Specimens B-1, B-2 and B-4 were 268, 252 and 102 kN respectively. The end and intermediate diaphragms were 200 and 90 mm thick respectively. Embedment connections were provided between the concrete flanges and corrugated steel web. All specimens were simply supported over a span of 3600 mm and tested by non-reversed cyclic loading at mid-span to increasing ductility levels under displacement control. Load cells were used at the end of each tendon to monitor the variation of tendon force during tensioning and the subsequent loading test. Linear variable differential transformers (LVDTs) were used to measure displacements during the test. Strain gauges were provided on concrete surface and steel bars at selected sections for monitoring of strains. The specimens under test are shown in Fig. 2.

The material properties were determined as shown in Table 2. The Young's modulus and ultimate strength of AFRP ropes were respectively 126.5 GPa and 1248 MPa. In tests, the tendons usually broke at the anchorage.

3. Experimental and numerical investigation

3.1. Elastic behaviour

Consider for example a bridge of this type under a few point loads. While the pair of concrete flanges tends to deflect together in flexure as a smooth curve, the corrugated steel webs tend to deflect in shear as a connected series of straight line segments, thereby causing interaction between the structural components

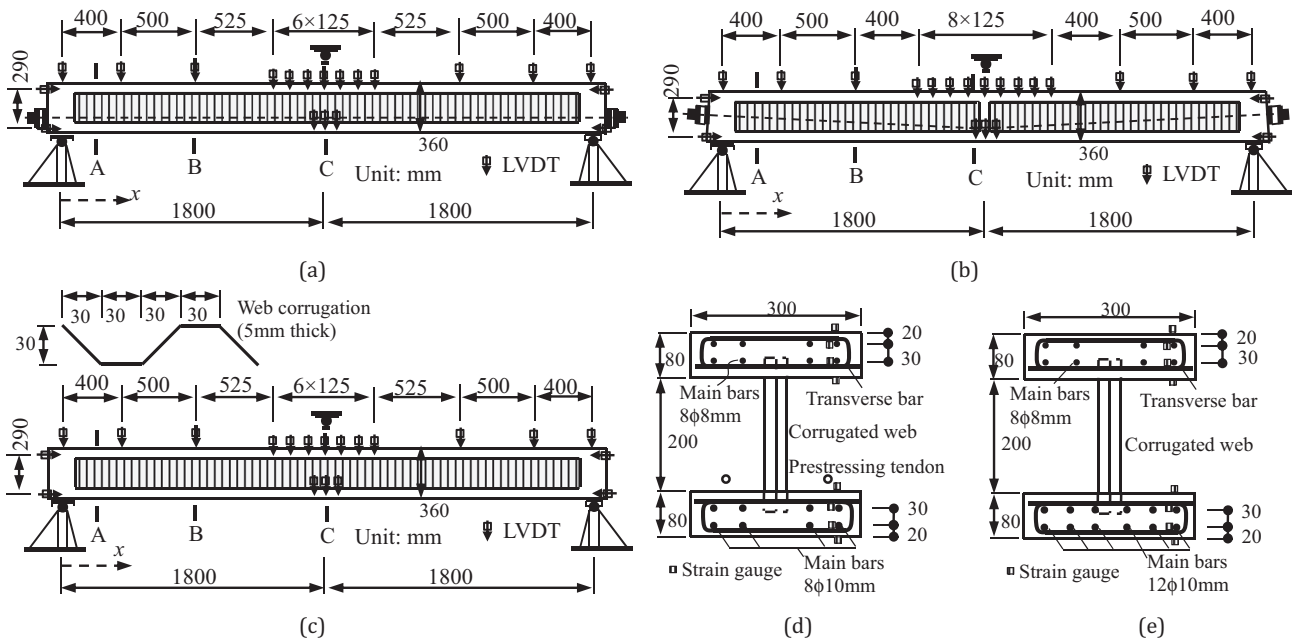


Fig. 1. Test specimens: (a) Specimen B-1; (b) Specimens B-2 and B-4; (c) Specimen B-3; (d) Section of Specimens B-1, B-2 and B-4; (e) Section of Specimen B-3.



Fig. 2. Specimens during test: (a) B-1; (b) B-2; (c) B-3; and (d) B-4.

Table 2
Material properties from tests (unit: MPa).

	Concrete				High yield steel bar (Ø10 mm)	Mild steel bar (Ø8 mm)	Steel strand (Ø12.7 mm)	AFRP rope (Ø13.5 mm)	Steel web
Specimen	B-1	B-2	B-3	B-4	All	All	B-1 & B-2	B-4	All
Initial Young's modulus	26107	27606	27329	27876	192277	208998	206780	126500	196056
Yield strength	–	–	–	–	559	423	–	–	267
Ultimate strength (cube/ cylinder)	54.3/ 47.5	61.3/ 52.2	62.9/ 53.8	55.3/ 47.0	672	499	2008	1248	399

[2,32]. The elastic behaviour can be analysed by the extended sandwich beam theory [2], which takes into account the diaphragms and interaction between shear deformation of steel webs and local bending of concrete flanges. The thin intermediate diaphragms are modelled as vertical flexural members, while the thick end diaphragms are treated as solid beam segments along the span. These effects induce secondary moment M_2 and shear force V_2 in the bridge, causing stress concentration in flanges around the diaphragms and point loads. In a section with negligible interaction effects, the strain variation is linear over the depth depending on the total curvature ϕ as shown in Fig. 3(a). In the presence of various interaction effects, apart from the primary curvature ϕ_1 , there is the secondary curvature ϕ_2 due to local bending of concrete flanges as shown in Fig. 3(b), and both of them contribute to the total curvature, i.e. $\phi = \phi_1 + \phi_2$. The secondary effects

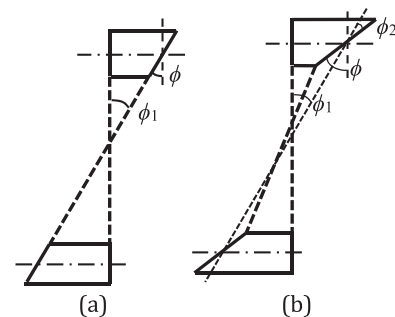


Fig. 3. Strain distribution over section depth: (a) Without interaction effects ($\phi_2 = 0$); and (b) With interaction effects ($\phi_2 \neq 0$).

are normally concentrated in the vicinity of point loads and diaphragms, and dissipate exponentially with distance.

The measured normal stresses at selected sections of Specimen B-1 at applied load 60.4 kN (at elastic stage) compare favourably with the results from sandwich beam model as shown Fig. 4, which show marked deviations from full-depth linear stress distributions at Section A (close to a diaphragm) and Section C (below a point load) due to secondary effects, but roughly full-depth linear stress distribution at Section B (away from any diaphragm and point load). The discrepancies between the experimental measurements and numerical results from sandwich beam model are mainly caused by the assumptions of negligible axial stiffness and vertical incompressibility of the corrugated steel webs as well as perfect connection between the flanges and steel web.

The measured curvature and slope along Specimen B-1 are compared with results from sandwich beam model in Figs. 5 and 6 respectively, which show significant secondary effects near the end diaphragms and point load. Referring to Fig. 3(b), the total curvature at a section can be estimated from the difference in strain gauge readings at the top and bottom surfaces of a flange and its thickness. However, because of the small but finite vertical compressibility of the corrugated steel webs, estimates of total curvature from the two flanges may differ slightly. Hence the total curvatures along the specimen were calculated as the average of estimated total curvatures from the two flanges. The primary curvatures were calculated based on the difference of average strains in flanges and the vertical distance between flange centroids. In the potential plastic zone around mid-span, the total curvatures were also calculated from the variation of deflection in three consecutive LVDTs. The slope at specimen end was calculated from measurements by a pair of horizontal LVDTs. The slope at location of a vertically mounted LVDT was calculated using readings from three consecutive LVDTs as

$$\theta_i = \left(\frac{x_{i+1} - x_i}{x_{i+1} - x_{i-1}} \right) \left(\frac{v_i - v_{i-1}}{x_i - x_{i-1}} \right) + \left(\frac{x_i - x_{i-1}}{x_{i+1} - x_{i-1}} \right) \left(\frac{v_{i+1} - v_i}{x_{i+1} - x_i} \right) \quad (1)$$

where θ_i , x_i and v_i were the slope, abscissa and deflection respectively at the i th location.

3.2. Moment-curvature relationship

The material laws considering strain reversal are adopted. Fig. 7 (a) shows the model for both unconfined and confined concrete comprising the stress-strain curve in compression developed by Attard and Setunge [33] and that in tension proposed by Carreira and Chu [34], and Guo and Zhang [35]. The stress-strain curve rec-

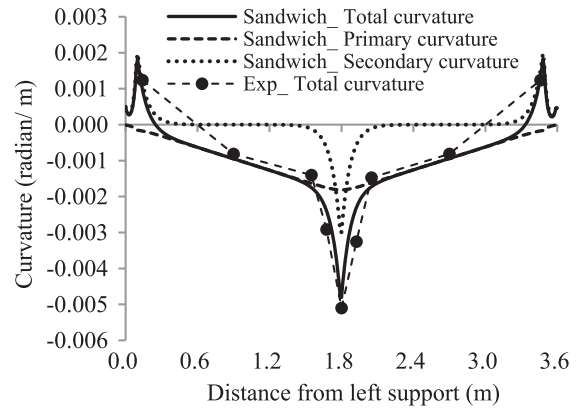


Fig. 5. Curvature along span of Specimen B-1.

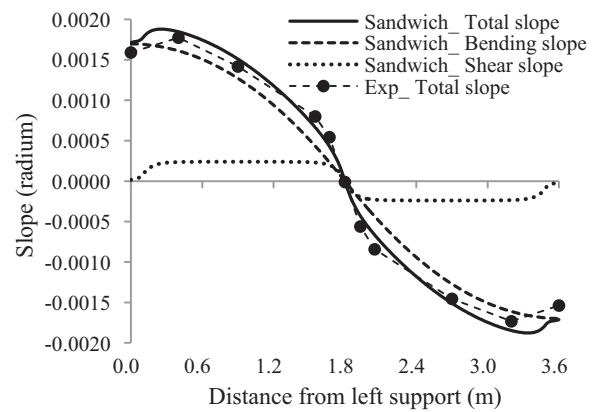


Fig. 6. Slope along span of Specimen B-1.

ommended by Mander et al. [36] is used for non-prestressed steel as shown in Fig. 7(b). The stress-strain formula for prestressing steel proposed by Menegotto and Pinto [37] is adopted here as shown in Fig. 7(c). The AFRP rope is linearly elastic up to failure and has no significant yielding.

According to the numerical study of Chen et al. [32] on the moment-curvature relationship of RC and PC sections of the bridge, the interaction effects increase the yield curvature significantly, but have insignificant effects on the ultimate curvature. The same approach is adopted here in view of its capability and efficiency.

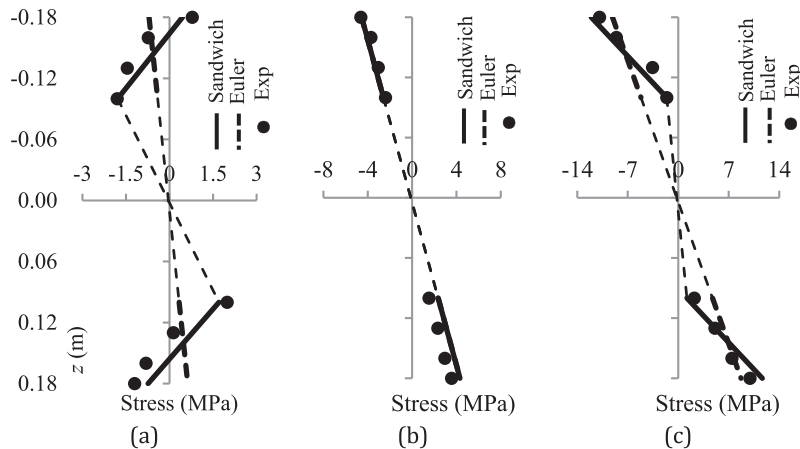


Fig. 4. Stress distribution of Specimen B-1: (a) Section A ($x = 0.14$ m); (b) Section B ($x = 0.9$ m); and (c) Section C ($x = 1.8$ m).

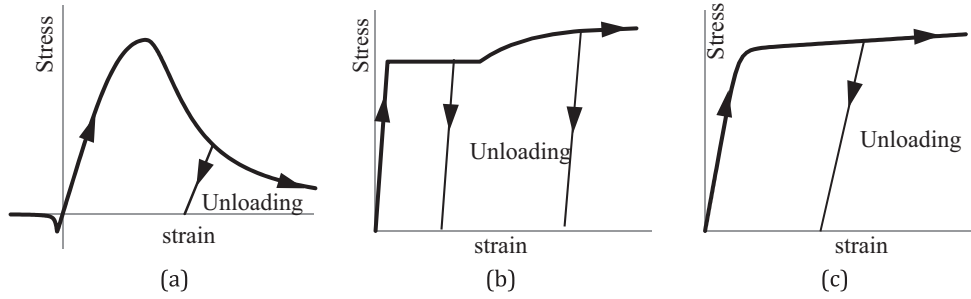


Fig. 7. Stress-strain curves of materials: (a) concrete; (b) non-prestressed steel; and (c) prestressing steel.

3.3. Full-range structural behaviour

3.3.1. Flexural failure mode

The measured load-deflection curves of Specimens B1 to B4 are shown in Fig. 8(a) to (d), respectively, with various observations identified. In the potential plastic zone around mid-span, tensile cracks appeared first in the lower flange. With the increase in loading, the tensile steel yielded and the neutral axis shifted towards the upper flange, placing the bottom of upper flange in tensile zone. Moreover, the secondary moment caused further tension and hence cracking at the bottom of upper flange. With the increase in displacement, tensile cracks in the upper flange gradually extended upwards, followed by the crushing of top concrete.

Shear crack also occurred in the upper flange later. The plastic hinge developed is shown in Fig. 9.

The ductility factor μ_d is defined in terms of the measured or calculated displacements as

$$\mu_d = d_u/d_y \tag{2}$$

where d_y is the equivalent yield displacement; and d_u is the ultimate displacement. The displacement can be deflection, slope or curvature. The definitions of equivalent yield and ultimate displacements by Park [38], and Du et al. [5] are adopted in this study. The equivalent yield displacement d_y is taken as the displacement at the hypothetical yield point of an equivalent bi-linear perfectly elastoplastic system with an elastic stiffness equal to the secant stiffness

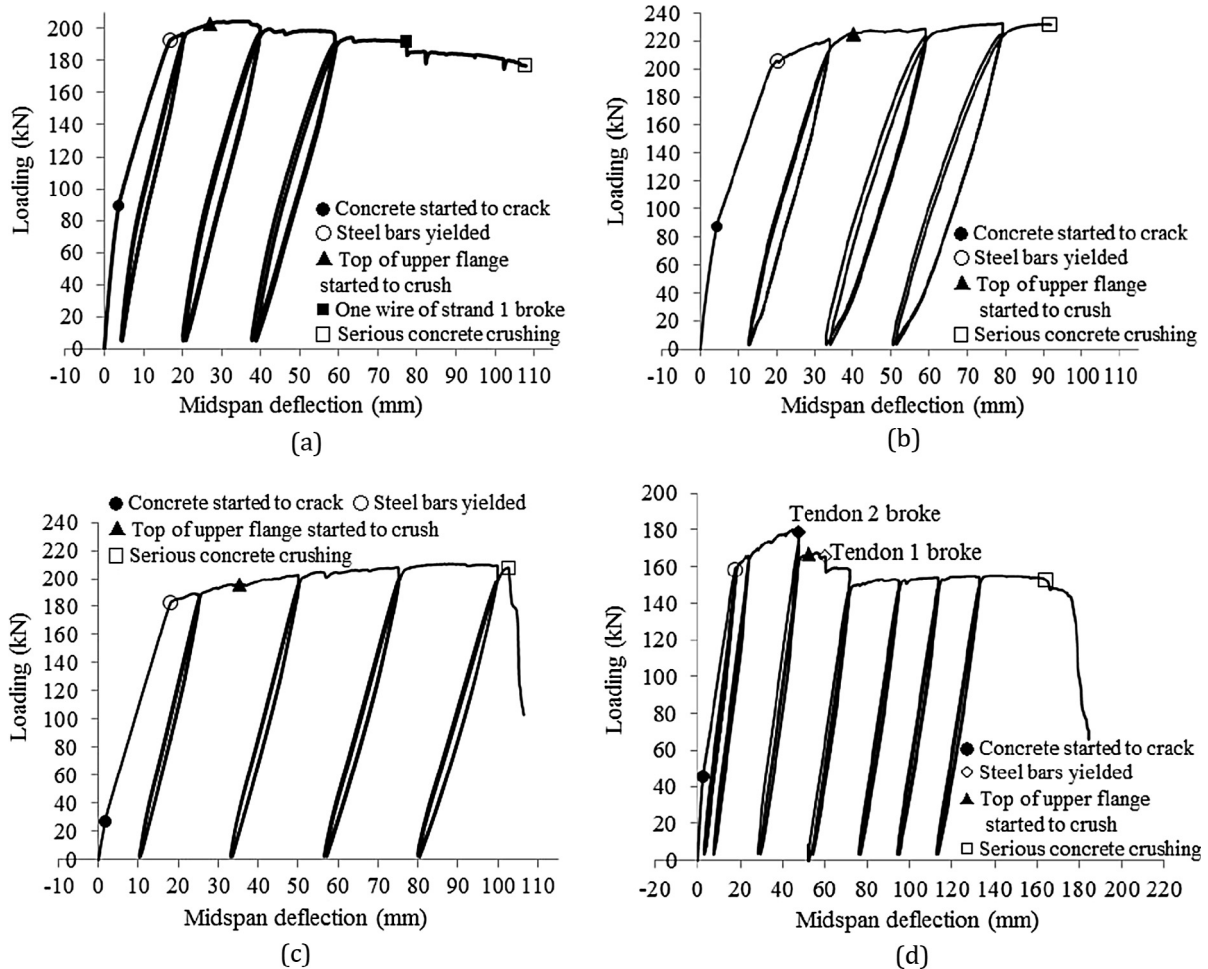


Fig. 8. Measured load-deflection curves: (a) Specimen B-1; (b) Specimen B-2; (c) Specimen B-3; and (d) Specimen B-4.

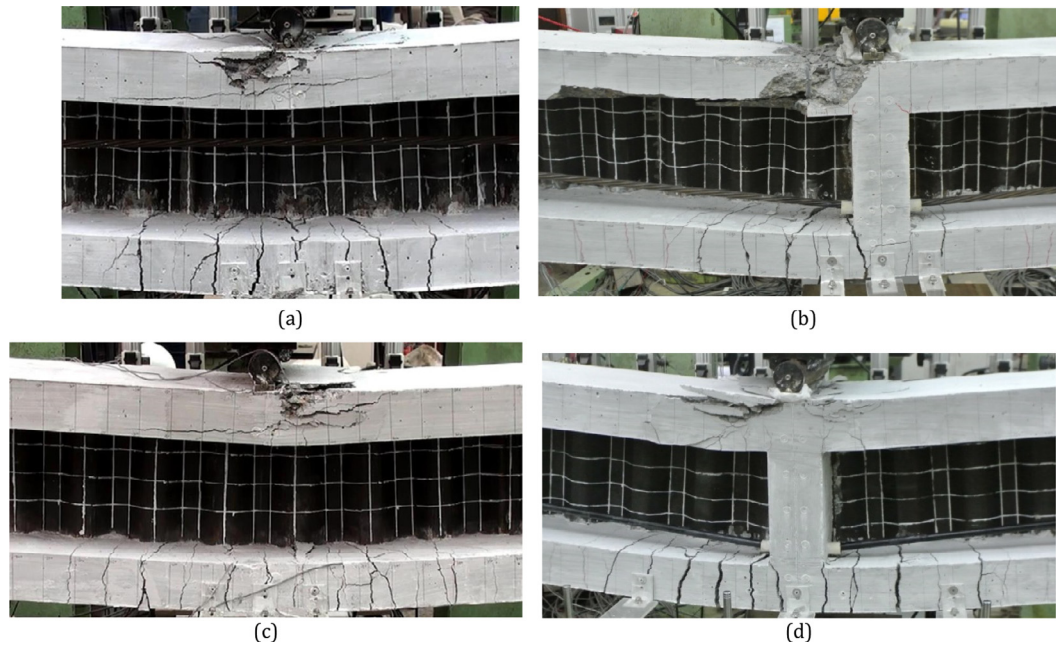


Fig. 9. Plastic hinge zones: (a) Specimen B-1; (b) Specimen B-2; (c) Specimen B-3; and (d) Specimen B-4.

of the structure at 75% of the peak resisting load and a yield load equal to the peak resisting load itself. The ultimate displacement d_u is taken as the displacement of the structure when the resisting load has dropped to 85% of the peak resisting load after passing the peak, or the displacement at which failure occurs, whichever is smaller. The measured ductility factors for mid-span deflection, specimen-end slope and curvature of the critical section are shown in Table 3. The critical sections of Specimens B-1 and B-3 are at the mid-span. For Specimens B-2 and B-4 with intermediate diaphragm at mid-span, the critical section is taken to be at either surface of the diaphragm. The ductility factor μ_θ for the specimen-end slope is very close to the ductility factor μ_v for the mid-span deflection. However, the curvature ductility factor μ_{cur} at the critical section is much higher in comparison, because it depends primarily on the sectional behaviour there, while the ductility factors for deflection and slope depend on the global structural behaviour.

The upper flange actually behaved like a strut under axial compression, shear and local bending. The axial load at ultimate P of the upper flange was estimated from the applied loading and tendon force, and tabulated in Table 3 as axial load level P/P_0 in terms of the axial compressive strength without bending P_0 as defined in Section 1. Because the AFRP tendons in Specimen B-4 ruptured quite early during the test as shown in Fig. 8(d), the specimen had lost all its prestress at ultimate. As the values of axial load level at ultimate of the upper flanges of Specimens B-1 and B-2 are larger than those of Specimens B-3 and B-4 without prestress, Specimens B-1 and B-2 failed suddenly after a long yield plateau.

3.3.2. Physical plastic hinge length l_{pc}

The physical length of the “full-depth plastic hinge” l_{pc} is determined from the measured curvature profile at ultimate along the span as the region with curvatures above the yield curvature ϕ_y without interaction effects. As the secondary effects caused by interaction are fairly localised, they are ignored here. Fig. 10 shows the measured total curvature profiles at different deflection ductility levels compared with the yield curvatures ϕ_y . The physical plastic hinge length l_{pc} can hence be determined from the measured curvature profile at deflection ductility factor at ultimate $\mu_{v,u}$. Table 4 shows that the mean values of physical plastic hinge length on one side of mid-span are around $1.55d$ for Specimens B-1 and B-2, and around $1.25d$ for Specimens B-3 and B-4, where d is the effective section depth of test specimens.

3.3.3. Critical region length l_c

The interaction between the shear deformation of corrugated steel webs and local bending of concrete flanges causes formation of local plastic hinge in the upper flange like a column plastic hinge. It is referred to as the “flange plastic hinge” here. It is essential to understand the interaction between the flange plastic hinge and full-depth plastic hinge, which takes place in the “critical region length” l_c where transverse reinforcement should be provided for effective confinement and strengthening of concrete. To avoid unnecessary proliferation of notations, the symbol l_c will be used to denote critical region length and the location (i.e. upper or lower flange) or its nature (i.e. interactive or not) will be stated.

Table 3
Measured ductility factors and prestressing force at ultimate limit state.

Specimen	Maximum loading (kN)	Yield deflection (mm)	Ultimate deflection (mm)	Yield end slope (radian)	Ultimate end slope (radian)	Yield curvature (radian/m)	Ultimate curvature (radian/m)	Ductility factors			Prestressing force at ultimate (kN)	Loading at ultimate (kN)	P/P_0 for upper flange at ultimate
								μ_v	μ_θ	μ_{cur}			
B-1	205	15.5	108.8	0.00637	0.0602	0.028	0.805	7.0	6.9	28.8	298	176	0.63
B-2	233	20.5	91.9	0.00948	0.0529	0.030	0.649	4.5	4.5	21.7	338	233	0.71
B-3	211	20.4	104.0	0.00887	0.0574	0.035	0.775	5.1	4.8	22.1	0	179	0.46
B-4	180	19.0	163.5	0.00722	0.0965	0.038	0.804	8.6	8.7	21.2	0	153	0.44

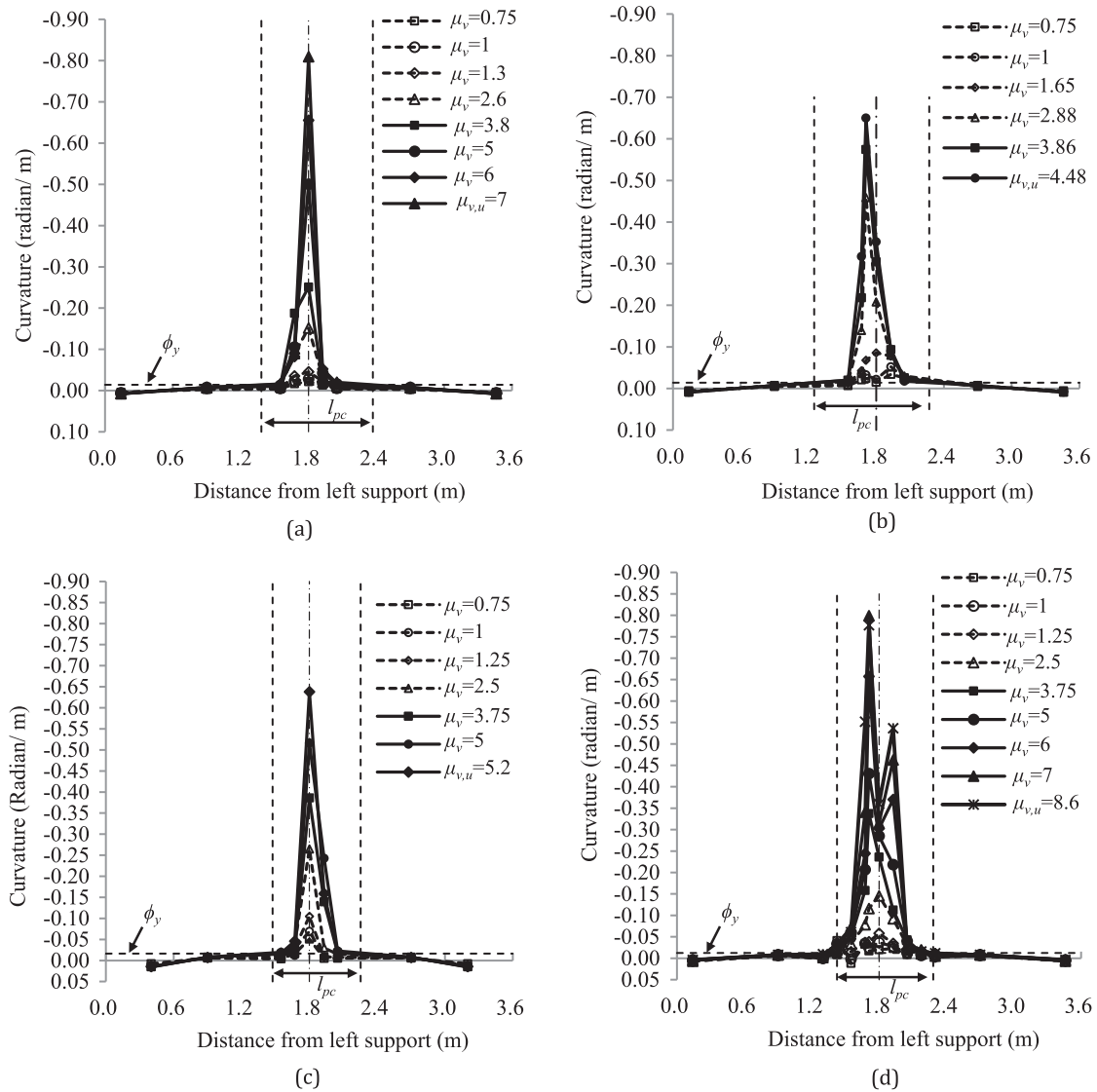


Fig. 10. Measured curvature: (a) Specimen B-1; (b) Specimen B-2; (c) Specimen B-3; and (d) Specimen B-4.

Table 4

Measured physical plastic hinge length l_{pc} , critical region length l_c and equivalent interactive plastic hinge length l_p .

Specimen	Total l_{pc} (mm)	Critical region length l_c (mm)					Measured interactive l_p (mm)	l_c/l_p			l_{pc}/l_p
		Upper flange		Lower flange		Interactive		Upper flange	Lower flange	Interactive	
		Left side	Right side	Left side	Right side						
B-1	986	150	–	220	210	238	1.22	3.50	1.94	8.03	
B-2	1019	160	–	290	105	310	1.23	3.03	2.38	7.82	
B-3	779	–	155	305	305	235	1.33	5.24	2.02	6.69	
B-4 ^a	857	165	155	320	300	490	1.46	2.84	2.24	3.92	

^a Upper flange plastic hinge formed on both sides of critical section.

The critical region length in the upper flange is closely related to the formation of flange plastic hinge, while the critical region length in the lower flange is closely related to cracking associated with the full-depth plastic hinge. By visual inspection, the critical region length in the upper flange can include regions having [29]: (a) spalling of concrete cover; (b) penetration of spalling into concrete core region; (c) local buckling of longitudinal steel; and (d) tensile cracks at flange bottom. In the early part of inelastic stage, both the number and width of cracks in the critical region

of lower flange increased. Afterwards, the load remained stable with the increase in displacement, while some cracks in the critical region widened significantly. Hence, the critical region length in the lower flange can include the region which suffers from significant tensile cracking [29]. After finishing the tests as described in Fig. 8, all the loose concrete pieces were removed to expose the degree of damage before taking photographs. The observed critical regions of specimens are shown in Fig. 11, together with the estimated critical region lengths. The critical region lengths in the

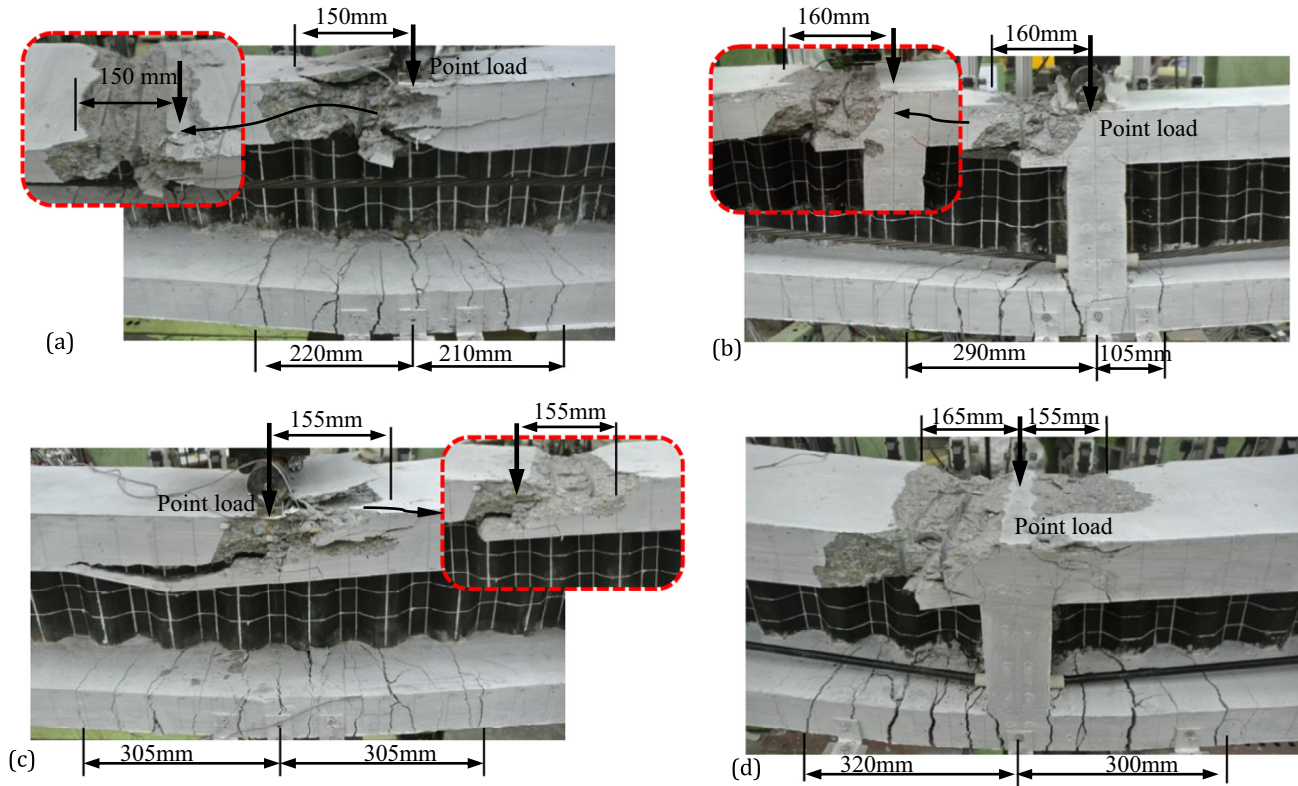


Fig. 11. Critical region length: (a) Specimen B-1; (b) Specimen B-2; (c) Specimen B-3; and (d) Specimen B-4.

upper flange of thickness t_u on one side of the point load at mid-span are all around $2.0t_u$ (i.e. 160 mm) as shown in Table 4. However, the critical region lengths in the lower flange on one side of mid-span vary much from $0.32d$ (i.e. 105 mm) to $0.98d$ (i.e. 320 mm). Considering the upper flange as a column due to compression caused by global bending, its critical region length was estimated as $2.0h$ according to Pam and Ho [29], which was consistent with that of Paultre et al. [31], but it was prescribed conservatively as $3.0h$ according to NZS 3101 [30]. Apparently, in the presence of extra confinement effect provided by the point load and/or diaphragm, and hence possible enhancement of flexural strength and ductility there [11], the critical region might not be symmetrical as summarised in Table 4. The centre of critical region was up to 80 mm shifted from mid-span.

The interaction between the critical region lengths in the upper and lower flanges results in an “interactive critical region length” that can be estimated from the measured slope profiles considering the specific boundary conditions. The slope profiles at different deflection ductility levels are shown in Fig. 12. The variations of end slope with the applied loading are plotted in Fig. 13, from which the corresponding yield slopes θ_y and ultimate slopes θ_u can be identified by the procedure described in Section 3.3.1. With the increase in imposed displacement, plastic deformation mainly concentrated in the critical region around mid-span while the other parts had undergone relatively little deformation. Hence an approximate method to estimate the boundary of critical region is to identify the section that has sustained a rotation equal to the yield slope θ_y assuming that the part outside the critical region can be taken as roughly straight. The interactive critical region length l_c of the beam can hence be determined accordingly from Fig. 12. Table 4 shows that the average interactive critical region length is about $3.3t_u$ for Specimens B-1 to B-3 with the plastic hinge formed only on one side of mid-span, and $6.1t_u$ for Specimen B-4 with a plastic hinge fully formed on both sides of mid-span,

where t_u is the thickness of upper flange. However, the critical region lengths in the lower flange are more variable. The critical region lengths in upper flanges of Specimens B-1 to B-3 are around half of that of Specimen B-4. It shows that the critical region in the upper flange governs the interactive critical region length.

3.3.4. Equivalent interactive plastic hinge length l_p

For simplified analysis of conventional beams or columns, the elastic curvature is often assumed to be distributed linearly from yield curvature at the critical section to zero at the free member end [11]. However, the curvature at the present specimen end was not zero but substantially reversed due to the diaphragm effects as shown in Fig. 5. Hence the “equivalent interactive plastic hinge length” l_p can be solved from

$$\theta_{end} = (1/2)\phi_y(L/2) + (\phi_u - \phi_y)l_p - \phi_{2, dia-p}(1/\alpha) \quad (3)$$

where θ_{end} is the specimen-end slope at ultimate; ϕ_y is the yield curvature at the critical section without interaction effects; ϕ_u is the ultimate curvature at the critical section; L is the span; $\phi_{2, dia-p}$ is the peak secondary curvature around the end diaphragm; α is a parameter to reflect the effects of interaction and diaphragm [2,32]; and the third term on the right-hand side is the integral of secondary curvature around the end diaphragm along the span [32].

The equivalent interactive plastic hinge length l_p so obtained depends on the interaction between the flange and full-depth plastic hinges, over which the plastic curvature is assumed to be constant at the peak value. Table 4 shows that the equivalent interactive plastic hinge lengths are around $1.5t_u$ for Specimens B-1 to B-3 with the flange plastic hinges formed only on one side of mid-span, and $2.7t_u$ for Specimen B-4 with a fully developed flange plastic hinge that is around twice of those for Specimens B-1 to B-3. Moreover the interactive critical region length l_c of Specimen B-4 is also around twice of those of Specimens B-1 to

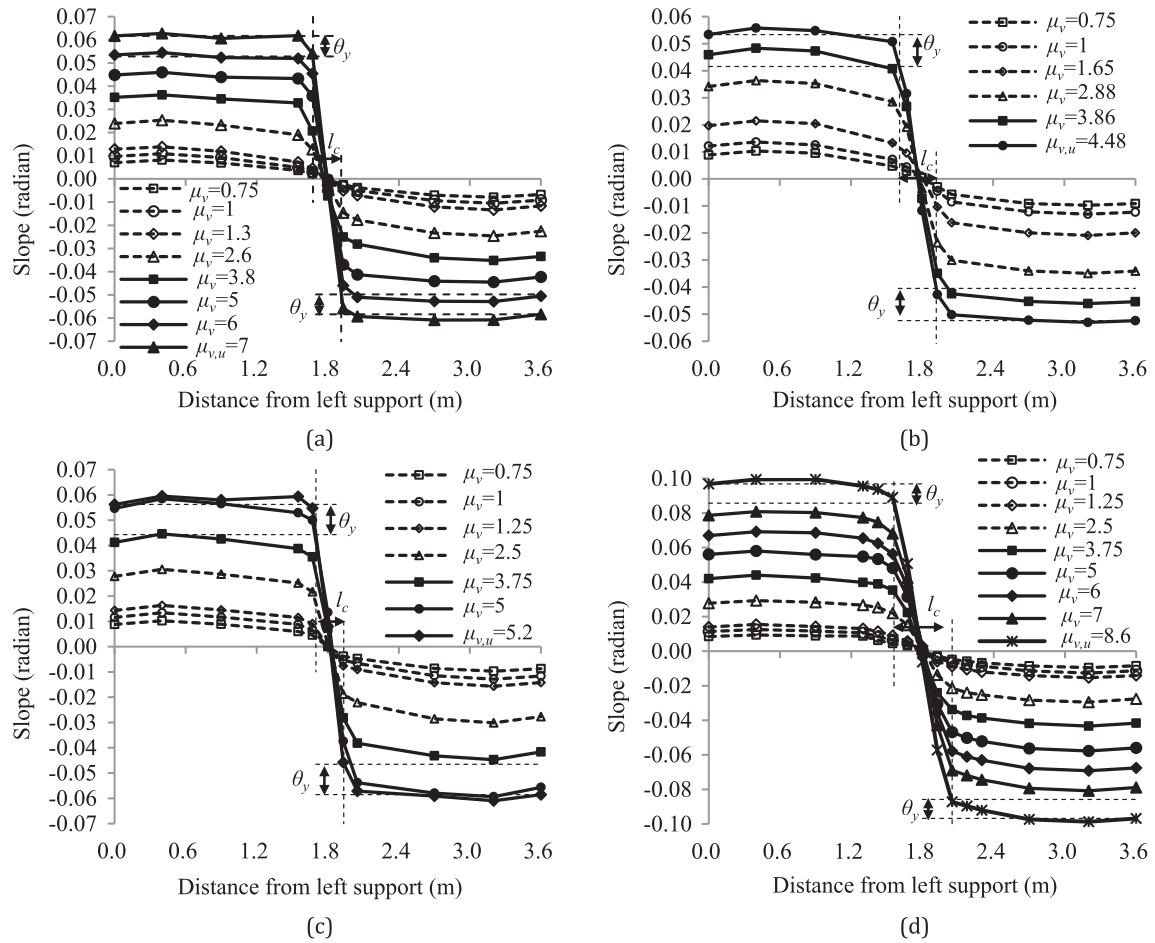


Fig. 12. Measured slope: (a) Specimen B-1; (b) Specimen B-2; (c) Specimen B-3; and (d) Specimen B-4.

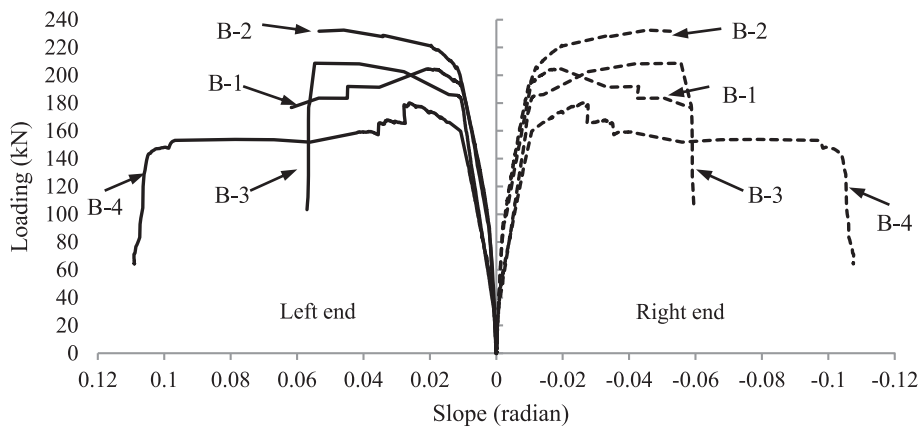


Fig. 13. Measured variation of end slope with applied loading.

B-3. Hence one may conclude that the flange plastic hinge governs the equivalent interactive plastic hinge length.

While the flange plastic hinges of Specimens B-1 to B-3 formed only on one side of mid-span, that of Specimen B-4 formed on both sides. Similar phenomena were also observed by Mendis [24] in the RC beam specimens tested, possibly due to inhomogeneity of concrete. Such variations in the extent and location of plastic hinge formation are more significant in this type of bridges. Hence, it is more conservative in design to assume the flange plastic hinge to

form only on one side of the critical section for lower energy dissipation.

Owing to the variation of flange plastic hinges, the total interactive critical region length, equivalent interactive plastic hinge length, specimen-end slopes and mid-span deflection of Specimen B-4 are around twice of those of Specimens B-1 to B-3, although the ultimate curvatures at critical sections of all specimens are quite similar. However, the physical plastic hinge lengths and critical region lengths in the lower flange are also more variable.

3.3.5. Relationship between various plastic hinge lengths and critical region lengths

Table 4 shows that the equivalent interactive plastic hinge length l_p is closely related to both the critical region length in the upper flange and the interactive critical region length, which are reflected by the ratios l_c/l_p clustering around 1.3 and 2.2 respectively. However, the physical plastic hinge lengths l_{pc} and critical region lengths l_c in the lower flange are not much related to the equivalent interactive plastic hinge length l_p . The results show that the plastic behaviour was mainly governed by the performance of the plastic hinge of the upper flange.

The relationship between various plastic hinge lengths and critical region lengths is summarized schematically in Fig. 14 for better understanding. Fig. 14(a) shows schematically the relationship between various estimates of plastic hinge length as well as the equations for estimation. The plastic hinge in the upper flange that results from local bending and the axial compression caused by global bending is relatively small, as compared to the bigger full-depth plastic hinge length characterized by significant tensile cracking in the lower flange. The left column in the block diagram in Fig. 14(b) shows that the equivalent interactive plastic hinge length results from the interaction between the flange plastic hinge and full-depth plastic hinge, which is based on observations and calculations. To ensure safety against various failure modes, proper reinforcement should be provided over the interactive critical region length according to the right column of the block diagram, which also depends on the interaction between the critical region lengths of both flanges.

3.3.6. Use of existing formulae on equivalent plastic hinge lengths

In Table 5, the measured equivalent interactive plastic hinge lengths l_p on one side of critical section are compared with the equivalent flange plastic hinge lengths calculated from empirical expressions for columns as shown in Table 1. The large scatter of estimates may be caused by the limited specimens tested and different emphases of existing formulae. Logically, the equivalent

flange plastic hinge length should be less than both the critical region length l_c of upper flange and the equivalent interactive plastic hinge length l_p . Hence, for the tested specimens, estimates of the equivalent flange plastic hinge length using formulae proposed by Baker [12], Park et al. [17], Sheikh and Khoury [20], Bayrak and Sheikh [21], Mendis [24] and Subramanian [27] are possible choices because they fall into the suitable range. The P/P_0 ratios at ultimate of the upper flanges of the specimens are comparable to the columns tested under high axial load by Sheikh and Khoury [20], and Bayrak and Sheikh [21], i.e. 0.36–0.63. Incidentally, the P/P_0 ratios of specimens tested by Park et al. [17] and Mendis [24] are generally lower than those of the upper flanges of the present specimens. The expression of Subramanian [27], combining those proposed by Baker [12], and Bae and Bayrak [25], takes into account the axial load level, strength of concrete and shear span ratio. Hence, the formulae of Sheikh and Khoury [20], Bayrak and Sheikh [21], and Subramanian [27] are considered more appropriate for application to the upper flanges of the present specimens. They also give estimates of equivalent flange plastic hinge length close to one another at around $1.0t_u$ (80 mm). This initial estimate of equivalent flange plastic hinge length can therefore be adopted in this study.

In Table 6, the measured equivalent interactive plastic hinge lengths l_p on one side of critical section are compared with estimates of the equivalent full-depth plastic hinge length obtained from the empirical expressions for beams in Table 1. All the predictions by empirical formulae are much higher than the measured equivalent interactive plastic hinge lengths l_p . Obviously, the equivalent full-depth plastic hinge length should be larger than the equivalent interactive plastic hinge length l_p (because of the simplifying assumption that the plastic curvature is constant at the peak value) but smaller than the measured critical region length of lower flange as shown in Table 4. Hence, for the present specimens, the equivalent full-depth plastic hinge lengths proposed by Baker [12], Sawyer [14] and Mattock [16] are acceptable because they fall into the suitable range. As the formula proposed

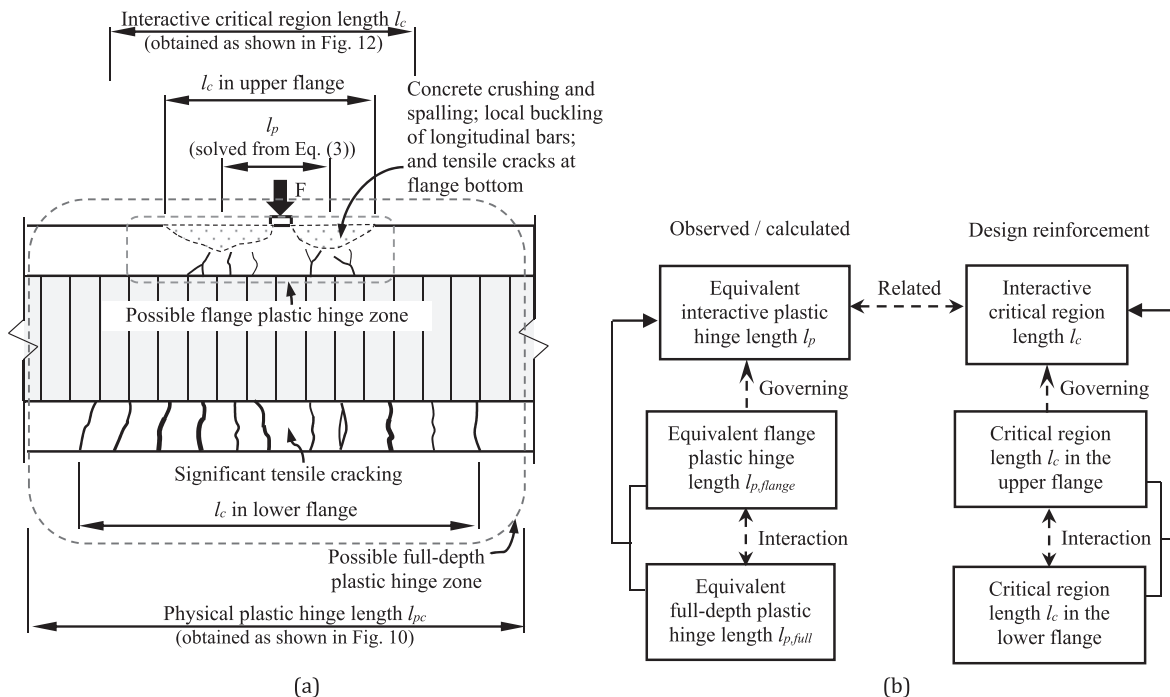


Fig. 14. Relationship between various plastic hinge lengths and critical region lengths: (a) estimates; and (b) relationship.

Table 5
Comparison of empirical estimates of flange plastic hinge length on one side of critical section (mm).

Specimen	Measured interactive l_p	Baker [12]	Baker and Amari-kone [13]	Sawyer [14]	Park et al. [17]	Park [18]	Priestley and Park [19]	Sheikh and Khoury [20]	Bayrak and Sheikh [21]	Mendis [24]	Panagiotakos and Fardis [23]	Bae and Bayrak [25]	Berry et al. [26]	Subramanian [27]
B-1	123	52	455	148	40	192	218	80	72–80	32	395	273	140	95
B-2	130	45	364	148	40	192	218	80	72–80	32	395	312	137	82
B-3	116	39	348	148	40	192	218	80	72–80	32	395	180	136	71
B-4 ^a	219/2	47	426	148	40	192	218	80	72–80	32	395	169	139	86

^a Upper flange plastic hinge formed on both sides of critical section.

by Baker [12] takes into account the axial load level, its estimates are the closest to the equivalent full-depth plastic hinge length obtained in this study.

3.4. Interaction between flange plastic hinge and full-depth plastic hinge

As elaborated in Sections 3.3.3–3.3.5, the flange plastic hinge governs the full-range structural behaviour of the bridge, indicating that the equivalent interactive plastic hinge length l_p is close to the equivalent flange plastic hinge length, while the effects of full-depth plastic hinge should also be taken into account. Hence, a simple formula for the equivalent interactive plastic hinge length l_p is proposed as

$$l_p = l_{p,flange} + 0.2l_{p,full} \tag{4}$$

where $l_{p,flange}$ is the equivalent flange plastic hinge length in accordance with Sheikh and Khoury [20], Bayrak and Sheikh [21] or Subramanian [27]; and $l_{p,full}$ is the equivalent full-depth plastic hinge length in accordance with Baker [12]. The coefficient 0.2 has been obtained by linear regression analysis of results. To evaluate the parameters in Eq. (4), different empirical formulae are used considering their respective applicability.

3.5. Simplified method for prediction of full-range structural behaviour

When the equivalent interactive plastic hinge length and sectional moment-curvature curves of a bridge are known, the deflection and slope can be obtained by integration of curvature along the span. With the use of external prestressing in the bridge, the structural behaviour is not just governed by that of individual sections but by the global behaviour. The relative slip between external tendons and deviators can be considered free in most practical cases. The model of Dall'Asta et al. [39] for externally prestressed Euler-Bernoulli beams is modified for this form of bridges. The profile of an external prestressing tendon is defined by the locations of end anchorages and intermediate deviators. Each location point \mathbf{c}_{0j} can be expressed as

$$\mathbf{c}_{0j} = x_j \mathbf{i} + e_j \mathbf{k} \tag{5}$$

where \mathbf{i} and \mathbf{k} are unit vectors parallel to x - and z -axes respectively; and x_j and e_j are the abscissa and eccentricity, respectively, of the j -th location point with a deviator or anchorage ($j = 0, 1, 2, \dots, n$). The initial total length of the tendon L_{t0} is given by

$$L_{t0} = \sum_{j=1}^n |\mathbf{c}_{0j} - \mathbf{c}_{0j-1}| \tag{6}$$

After deformation, the location point \mathbf{c}_{0j} moves to a new position \mathbf{c}_j of

$$\mathbf{c}_j = [x_j + u_j + e_j \varphi_j] \mathbf{i} + [e_j + v_j] \mathbf{k} \tag{7}$$

where u_j , v_j and φ_j are the displacements at abscissa x_j . The total length of the tendon after deformation L_t is given by

$$L_t = \sum_{j=1}^n |\mathbf{c}_j - \mathbf{c}_{j-1}| \tag{8}$$

The additional elongation ΔL_t of the external tendon is then obtained as $\Delta L_t = L_t - L_{t0}$, causing an additional strain of $\varepsilon_p = \Delta L_t / L_{t0}$. The stress and force of external tendon are then obtained according to its stress-strain curve and sectional area. According to the displacement of deviators and anchorages, the forces that the external tendon transmits to the bridge are obtained.

Table 6
Comparison of measured equivalent interactive plastic hinge length and application of existing formulae for beams to full-depth plastic hinge (one side of the critical section) (mm).

Specimen	Measured interactive l_p	Baker [12]	Sawyer [14]	Corley [15]	Mattock [16]	Panagiotakos and Fardis [23]
B-1	123	241	216	794	253	398
B-2	130	202	216	794	253	398
B-3	116	172	216	794	253	398
B-4 ^a	219/2	211	216	794	253	398

^a Upper flange plastic hinge formed on both sides of critical section.

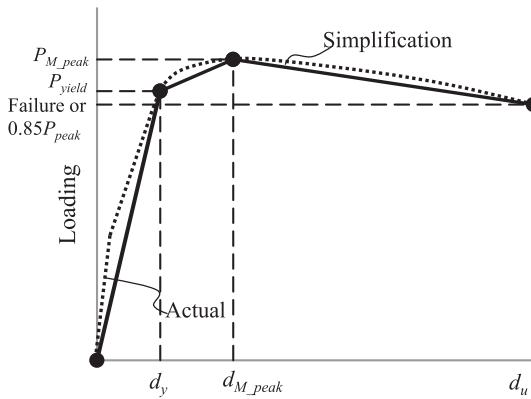


Fig. 15. Actual and simplified load-displacement curves.

In the proposed simplified method for prediction of full-range structural behaviour based on the concept of equivalent plastic hinge length, the second-order effects associated with external tendons are also considered. The load-displacement and load - tendon stress curves are modelled as tri-linear as shown in Fig. 15, where P_{yield} and P_{peak} are the yielding and ultimate loads respectively; and the subscript M_{peak} denotes the stage at which the moment-curvature curve reaches its peak. The first stage extends up to the yielding of tension steel. The second stage covers the

state when the moment-curvature curve of the critical section reaches the peak moment. The third stage describes the ultimate state prior to failure. Because of external prestressing, the ultimate load may not occur when the moment-curvature curve of the critical section reaches its peak. Instead the load may continue to rise with displacement, finally reaching the peak at the ultimate state, e.g. Specimen B-2, although it may fail due to concrete crushing anytime. In many cases, the tri-linear model is sufficiently accurate [11]. The pre-cracking and post-cracking parts of load-displacement relationship can be approximated by a straight line in the first stage up to the onset of yielding as shown in Fig. 8. The tri-linear model in Fig. 15 is an efficient approximation for the study of full-range structural behaviour. This simplified method is illustrated by a flowchart in Fig. 16.

Using the simplified method, the relationships between the load and mid-span deflection, specimen-end slope and tendon stress for Specimens B-1 and B-2 are predicted and compared with the measured hysteresis envelopes as shown in Fig. 17, which show reasonable agreement. Because of the confinement effect of the point load, the predicted ultimate displacements are slightly below the experimental results. The applied load of Specimen B-1 with straight tendons reaches the peak roughly when the critical section reaches the peak of moment-curvature curve. However, the applied load of Specimen B-2 with deflected tendons reaches its peak at the ultimate stage, when the deflected tendons take up increasing load with the failure of the plastic hinge. Therefore

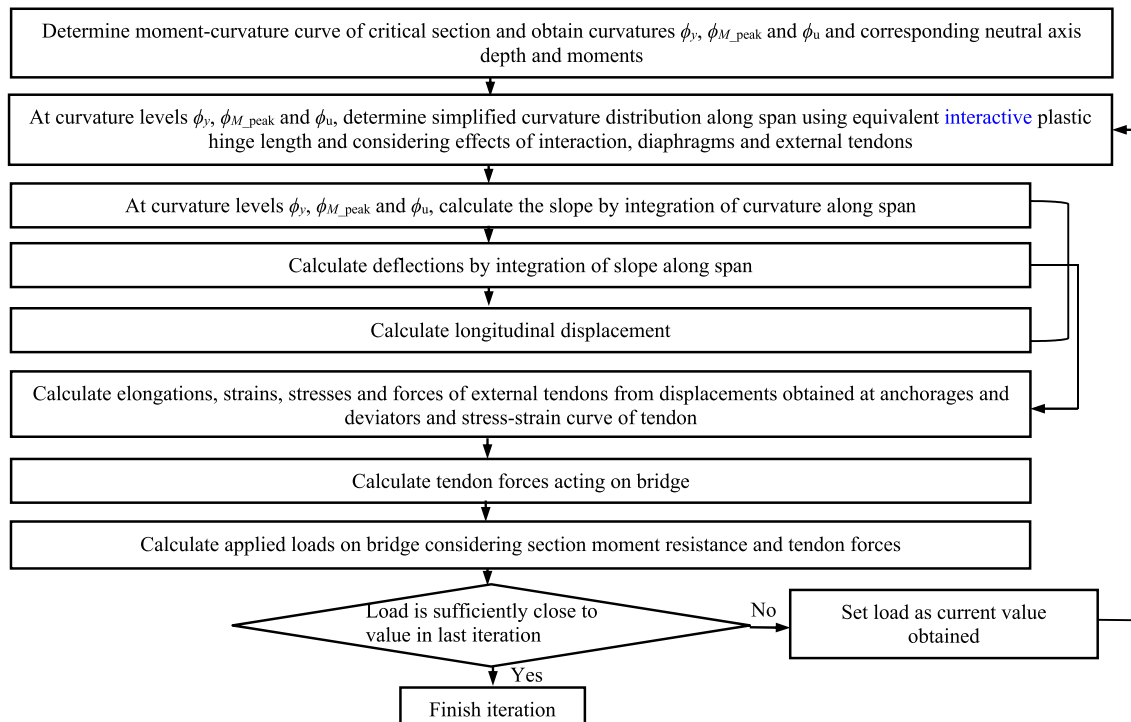


Fig. 16. Flowchart for simplified method to predict full-range structural behaviour of bridge.

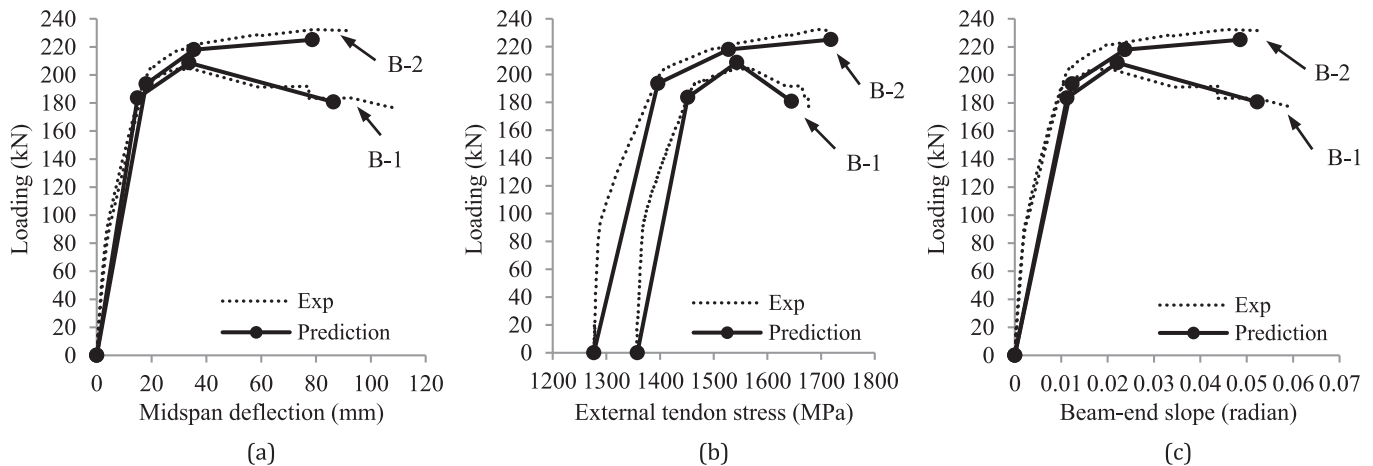


Fig. 17. Prediction of full-range structural behaviour of Specimens B-1 and B-2: (a) load vs. mid-span deflection; (b) load vs. tendon stress; and (c) load vs. specimen-end slope.

the ductility, deformability and ultimate load of a bridge depend not only on the performance of concrete flanges and tendon arrangement, but also on any possible premature failure such as tendon rupture or concrete crushing. In this example, the predicted equivalent flange plastic hinge length $l_{p,flange}$ is obtained in accordance with Sheikh and Houry [20]. To determine the displacements corresponding to the peak moment, the curvature at the peak moment is assumed to be distributed uniformly over the equivalent interactive plastic hinge length in the analysis.

4. Design recommendations

To estimate the ultimate displacement and load, it is conservative to assume the plastic hinge to form only on one side of the critical section; otherwise the strength and ultimate displacement will be over-estimated. The equivalent interactive plastic hinge length l_p may be predicted by the proposed formula (i.e. Eq. (4)). The critical region length l_c in the upper flange is about twice the flange thickness, where transverse reinforcement should be provided to confine and strengthen concrete properly, prevent buckling of compression steel and enhance ductility [40]. The arrangement of external tendons also affects the ductility, deformability and ultimate load of the bridge. Providing more intermediate deviators normally reduces the secondary effects and improves the ductility and deformability.

5. Conclusions

Owing to the presence of prestressing tendons and shear-deformable corrugated steel webs with negligible axial stiffness in this type of bridges, flange plastic hinge and full-depth plastic hinge may form and interact with each other. Experimental results show that the equivalent interactive plastic hinge length, critical region length and plastic behaviour are mainly governed by the formation of flange plastic hinge. Using the equivalent interactive plastic hinge length estimated by an empirical formula, a simplified method is proposed to predict the full-range structural behaviour and load-carrying capacity of the bridge. Based on the numerical and experimental study, some design recommendations are provided.

Acknowledgements

The work reported in this paper is supported by the Research Grants Council (RGC) of the Hong Kong Special Administrative Region, China (RGC Project No. HKU 710111E).

References

- [1] Machindamrong C, Watanabe E, Ustunomiya T. Analysis of corrugated steel web girders by an efficient beam bending theory. *Struct Eng/Earthquake Eng, JSCE* 2004;21(2):131s–42s.
- [2] Chen XC, Bai ZZ, Au FTK, Zeng Y. An extended sandwich theory for prestressed concrete bridges with corrugated steel web(s). Report of IABSE Conference on “Elegance in Structures”, Nara, 13–15 May 2015b. p. 270–271 and No. IA-22 in CD.
- [3] Ho JCM, Pam HJ. Inelastic design of low-axially loaded high-strength reinforced concrete columns. *Eng Struct* 2003;25:1083–96.
- [4] Au FTK, Du JS, Cheung YK. Service load behavior of unbonded partially prestressed concrete members. *Mag Concr Res* 2005;57(4):199–209.
- [5] Du JS, Au FTK, Cheung YK, Kwan AKH. Ductility analysis of prestressed concrete beams with unbonded tendons. *Eng Struct* 2008;30(1):13–21.
- [6] Chou CC, Chang HJ, Hewes JT. Two-plastic-hinge and two dimensional finite element models for post-tensioned precast concrete segmental bridge columns. *Eng Struct* 2013;46:205–17.
- [7] Yang KH, Mun JH, Kim GH. Flexural behavior of post-tensioned normal-strength lightweight concrete one-way slabs. *Eng Struct* 2013;56:1295–307.
- [8] Di Ludovico M, Polese M, d’Aragona MG, Prota A, Manfredi G. A proposal for plastic hinges modification factors for damaged RC columns. *Eng Struct* 2013;51:99–112.
- [9] Lee C, Shin S, Lee S. Modelling of load-deflection of concrete beams internally prestressed with unbonded CFRP tendons. *Mag Concr Res* 2015;67(13):730–46.
- [10] Hines EM, Restrepo JI, Seible F. Force-displacement characterization of well-confined bridge piers. *ACI Struct J* 2004;101(4):537–48.
- [11] Park R, Paulay T. Reinforced concrete structures. New York: John Wiley & Sons; 1975.
- [12] Baker ALL. Ultimate load theory applied to the design of reinforced and prestressed concrete frames. London: Concrete Publications Ltd.; 1956.
- [13] Baker ALL, Amarakone AMN. Inelastic hyperstatic frames analysis. In: Proceedings of the international symposium on the flexural mechanics of reinforced concrete, ASCE-ACI, Miami, November 1964. p. 85–142.
- [14] Sawyer HA. Design of concrete frames for two failure states. Proceedings of international symposium on the flexural mechanics of reinforced concrete, ASCE-ACI, Miami; 1964: p. 405–31.
- [15] Corley GW. Rotation capacity of reinforced concrete beams. *J. Struct. Div., ASCE*; 1966;92(10):121–46.
- [16] Mattock AH. Discussion of “rotational capacity of reinforced concrete beams” by W. D. G. Corley. *J Struct Div, ASCE* 1967;93(2):519–22.
- [17] Park R, Priestley MJN, Gill WD. Ductility of square-confined concrete columns. *J Struct Div, ASCE* 1982;108ST(2):929–50.
- [18] Priestley MJN, Park R. Strength and ductility of concrete bridge columns under seismic loading. *ACI Struct J* 1987;84(1):61–76.
- [19] Paulay T, Priestley MJN. Seismic design of reinforced concrete and masonry buildings. New York: John Wiley and Sons; 1992.
- [20] Sheikh SA, Houry SS. Confined concrete columns with stubs. *ACI Struct J* 1993;90(4):414–31.
- [21] Bayrak O, Sheikh SA. High-strength concrete columns under simulated earthquake loading. *ACI Struct J* 1997;94(6):708–22.
- [22] Coleman J, Spacone E. Localization issues in force-based frame elements. *J Struct Eng, ASCE* 2001;127(11):1257–65.
- [23] Panagiotakos TB, Fardis MN. Deformations of reinforced concrete members at yielding and ultimate. *ACI Struct J* 2001;98(2):135–48.
- [24] Mendis P. Plastic hinge lengths of normal and high-strength concrete in flexure. *Adv Struct Eng* 2001;4(4):189–95.
- [25] Bae SJ, Bayrak O. Plastic hinge length of reinforced concrete columns. *ACI Struct J* 2008;105(3):290–300.

- [26] Berry MP, Lehman DE, Lowes LN. Lumped-plasticity models for performance simulation of bridge columns. *ACI Struct J* 2008;105(3):270–9.
- [27] Subramanian N. Discussion of "Plastic Hinge Length of Reinforced Concrete Columns" by Sungjin Bae and Oguzhan Bayrak. *ACI Struct J* 2009;106(2), Disc. 105–S28:233–4.
- [28] Youssf O, ElGawady MA, Mills JE. Displacement and plastic hinge length of FRP-confined circular reinforced concrete columns. *Eng Struct* 2015;101:465–76.
- [29] Pam HJ, Ho JCM. Length of critical region for confinement steel in limited ductility high-strength reinforced concrete columns. *Eng Struct* 2009;31:2896–908.
- [30] Standards New Zealand. NZS 3101. The design of concrete structures. Concrete Structures Standard, Part 1: Code of Practice; 2006. p. 284.
- [31] Paultre P, Legeron F, Mongeau D. Influence of concrete strength and transverse reinforcement yield strength on behavior of high-strength concrete columns. *ACI Struct J* 2001;98(4):490–501.
- [32] Chen XC, Au FTK, Bai ZZ, Li ZH, Jiang RJ. Flexural ductility of reinforced and prestressed concrete sections with corrugated steel webs. *Comput Concr* 2015;16(4):625–42.
- [33] Attard MM, Setunge S. The stress-strain relationship of confined and unconfined concrete. *ACI Mater J* 1996;93(5):432–42.
- [34] Carreira DJ, Chu KH. The moment-curvature relationship of reinforced concrete members. *ACI Struct J* 1986;95:725–39.
- [35] Guo ZH, Zhang XQ. Investigation of complete stress-deformation curves for concrete in tension. *ACI Mater J* 1987;84(4):278–85.
- [36] Mander JB, Priestley MJN, Park R. Seismic design of bridge piers. Research report 84-2, University of Canterbury, Christchurch; 1984.
- [37] Menegotto M, Pinto PE. Method of analysis for cyclically loaded R.C. plane frames. IABSE Preliminary Report for Symposium on Resistance and Ultimate Deformability of Structures Acted on by Well Defined Repeated Loads, Lisbon; 1973.
- [38] Park R. Ductility evaluation from laboratory and analytical testing. Proceedings of the 9th world conference on earthquake engineering, vol. VIII, 2–9 August 1988, Tokyo—Kyoto, Japan; 1988. p. 605–16.
- [39] Dall'Asta A, Ragni L, Zona A. Analytical model for geometric and material nonlinear analysis of externally prestressed beams. *J Eng Mech* 2007;133(1):117–21.
- [40] Base GB, Read JB. Effectiveness of helical binding in the compression zone of concrete beams. *J ACI* 1965;62(7):763–81.